Available online at www.sciencedirect.com

ScienceDirect

Procedia Structural Integrity 24 (2019) 636–650

Structural Integrity Procedia

www.elsevier.com/locate/procedia

AIAS 2019 International Conference on Stress Analysis

Novel method of utilizing Acoustic Emission Parameters for Damage Characterization in Innovative Materials

Claudia Barile[a]*, Caterina Casavola[a], Giovanni Pappalettera[a], Vimalathithan Paramsamy Kannan[a]

[a]*Dipartimento di Meccanica, Matematica e Management, Politecnico di Bari, Viale Japigia 182, 70126 – Bari, Italia*

Abstract

Acoustic emission technique is used to characterize the damage modes in AlSi10Mg specimens prepared using Selective Laser Melting technique. Three specimens built in different orientations with respect to the building platform were tested. The parameter-based acoustic parameter, peak amplitude was clustered to identify the different damage zones. Davies-Bouldin Index (DBI) is used to optimize the number of clusters and k-means++ algorithm was used to cluster the peak amplitude data. The linear relation between two other acoustic parameters, cumulative counts and cumulative energy, is used to exploit the damage mode under the loading condition. The slope of the linear relation, b_{AE} is estimated for this study. Finally, the signal-based acoustic parameter, wavelets are transformed using Continuous Wavelet Transform (CWT) and Wavelet Packet Transform (WPT) in an attempt to identify the frequency bands associated with the damage modes. With the aid of proper in-situ characterization tool to support the Acoustic Emission Technique, it can be a powerful tool in damage monitoring and characterization in metal specimens.

Keywords: Wavelet Transform; Acoustic Emission; b-value; Pattern recognition/clustering algorithms; Selective Laser Melting; AlSi10Mg

* Corresponding author. Tel. +39 080 596 3209
E-mail address: claudia.barile@poliba.it

10.1016/j.prostr.2020.02.056

1. Introduction

Acoustic Emission (AE) technique has been evolving rapidly over the last 3 or 4 decades. This passive evaluation technique is based on the transient elastic waves generated during a damage propagation in material. These events are termed as acoustic events (Grosse (2008)). Over the years, the researchers have used multiple characterization technique in using acoustic parameters for characterizing damage propagation. Acoustic counts have been used countless time in predicting the crack growth in metal specimens by Pascoe et. al (2018). Similarly, acoustic energy has been used by Pascoe et. al (2018), Barile et. al (2014), Barile et. al (2015) and Vshivkov et. al (2019), to identify the critical points of failure under loading. However, the real applications of the AE descriptors have never been explored; at least in metal specimens. For instance, the acoustic energy has been directly related to the strain energy of the material under loading in composites using Sentry Function, proposed by Minak and Zucchelli (2008).

The acoustic counts and energy have been used to predict the lifetime of a civil structure by Carpinteri and Lacidogna (2007). Moreover, the signal-based data such as peak frequency, frequency centroid and duration has been related successfully to different damage modes in fiber reinforced composites. This raises a question, why these parameters were not explored in metal specimens as efficiently they were in polymer composites and civil structures? The acoustic waves are transient in nature and in case of the signals generated in metal specimens, it is even narrow in the time-frequency band. Thus, so far, it has not been popularly used in metal specimens. Recently, Botvina and Tyutin (2019) used a novel approach to use the acoustic energy and counts for charactering damage stages under cyclic loading in metals. They also have used an entirely new acoustic parameter named as acoustic gap.

Moreover, a countable number of researchers have tried to use the signal-based data generated from acoustic waves. Everson and Cheraghi (1999) have analysed the acoustic waves generated during the drilling of metal specimens. These few research works have paved way for the exploration of different acoustic parameter in metal specimens. In this research work, a novel way of using the amplitude, energy, counts and signal-based wavelets are discussed. The aim of the work is to relate the AE descriptors with the different damage modes in metal specimens. For this purpose, three materials specimens build using Selective Laser Melting was were tested under tensile loading conditions. These three specimens are built along three different orientations with respect to the building platform. The acoustic waves generated during the tensile test were recorded and analysed using different techniques.

2. Materials and Methods

2.1. Methods

In this research work, three types of SLM specimens based on the directions in which they are built with respect to the building platform. The specimens used for this study are built along X, Y and 45° inclination. The feed material for the SLM process is AlSi10Mg, which is one of the popular alloys for aluminium castings. It has excellent casting properties owing to the formation of Mg_2Si precipitate. It has 11% Si in its composition and its presence makes it a hypoeutectic alloy. The presence of 0.45% of Mg improves the hardenability of the manufactured component. The other chemical compositions are provided in Table 1. The alloy has a low density 2.68 gm/cm^3 and a melting range between 570 ℃ and 590 ℃. As indicated by Kempen et. al (2012) and Tradowsky et. al (2016) The oxide layer forming naturally in this alloy serves as a good corrosion barrier. The building parameters of the SLM process are presented in Table 2.

Table 1. Chemical Composition of the Feed Material.

Element	Al	Si	Mg	Fe	N	O	Ti	Zn	Mn	Ni	Cu	Pb	Sn
Mass (%)	Bal*	11	0.45	<0.25	<0.2	<0.2	<0.15	<0.1	<0.1	<0.05	<0.05	<0.02	<0.02

**Balance percentage is Aluminium*

Table 2. SLM Process Building Parameters.

Parameter	Details
SLM System	RenAM 500M Industrial additive manufacturing system (Renishaw plc, Staffordshire, United Kingdom)
Laser type	Nd-YAG Solid-state
Power Output	400 W
Wavelength	1.064 µm
Spot Diameter	200 µm
Scanning Velocity of Laser	11 mm/s
Energy Density	2 J/mm^2
Thickness of Layer	20 µm

The specimens were not post-processed, since the scope of this research work is to relate the damage mechanisms under tensile loading with Acoustic Emission parameters.

2.2. Tensile Test Setup

The specimens were prepared according to ASTM E8M specimen. In the exact misposition along the length of the specimen, a uniaxial strain gauge was attached. The surface of the specimen was cleaned with acidic solution followed by neutralizing it with a base before ensuring the proper adhesion of the strain gauge to the surface. The test was carried out under displacement-controlled mode at a crosshead displacement rate of 1 mm/min. The test was carried out in INSTRON 1342-Servohydraulic loading machine with a maximum load capability of 10 kN.

2.3. Acoustic Emission Setup

To record the acoustic emission activity under loading, a wideband and lightweight miniature AE sensor was coupled to the surface of the specimen. The characteristics of the AE sensor is presented in Table 3. The sensor was coupled to the surface of the specimen through two couplants. First, silica gel was applied to the surface of the specimen. The silica gel provides the proper connection between the AE sensor and the specimen surface. It also facilitates the proper acquisition of AE signals without the interference of the reverberation frequency from the oscillating sensor crystal. Following this, a Kapton tape of thickness 0.03 mm was adhered to the surface. This is to prevent the interference of the strain gauge and the loading cell of the test setup from affecting the acquisition.

Table 3. Characteristics of AE sensor.

PICO Sensor Characteristics	
Peak Sensitivity	54 dB
Operating Frequency	250 – 750 kHz
Resonant Frequency	250 kHz
Operating Range	-65 ℃ to 177 ℃
Dimensions	3.94 mm x Ø 4.78 mm

It is experimentally proved by Finkel et. Al (2000) that the variation in thickness of the couplant and the surface roughness of the specimen can affect the recorded AE data. The Kapton tape not only prevents the interference signals but also, along with the silica gel, provides approximately a uniform couplant layer thickness between the specimen surface and the sensor crystal.

The sensor signals are amplified by 40 dB using 2/4/6-AST preamplifier. The signals are passed through a low-band filter of 1 kHz and high-band filter of 3 MHz before recording the acoustic event waveform at a length of 5K.

The waveforms are recorded at the rate of 1 MSPS. The parameter-based AE descriptors, peak amplitude, counts and energy are recorded and analysed for this study.

2.4. Clustering of AE data

Normally, the AE data clustering is popular in composite materials and has rarely been used in metal specimens, so far (Chai et. al (2017) and Bi et. al. (2015)). More importantly, the clustering or pattern recognition has never been used in damage identification under static loading of metals. One of the novelties of the work is to cluster the AE data generated in metal specimens to identify different regions of damage progression. Conventionally, the AE data are classified into different clusters based on the needs of the researchers. However, it has a major limitation that the optimum cluster in which the data can be classified has never been considered. In this research work, the Davies-Bouldin Index (DBI) has been calculated for the AE amplitude to identify the optimum number of clusters [16]. The DBI is a metric for calculating the optimum number of clusters prior to classifying the data using any clustering algorithm. The cluster number with the minimum DBI index is the optimum.

The clustering algorithm used in this study is the k-means++ algorithm. This algorithm classifies the input data into predefined number of clusters (k) according to the following procedure:

- Select a random point from the input dataset X. This random datapoint is considered as the first centroid (c_1).
- Compute the distance of all the datapoints from the centroid c_1. The distance between the centroid c_j and each datapoint m is stored as $d(x_m,c_j)$.
- The next centroid is selected with the following probability in random from the dataset X.

$$d^2(x_m, c_1) / \sum_{j=1}^{n} d^2(x_j, c_1), \tag{1}$$

- Choose centre j by computing the distance between each datapoint of each dataset and the respective centroid.
- Assign each datapoint to the closest centroid.
- Repeat Steps 4 and 5 until all centroids k are chosen.
- Calculate datapoint to cluster centroid distance for all the datapoints with respect to their assigned centroid.
- Calculate the average of the datapoints in each cluster to obtain new (or optimal) centroid locations.
- Repeat Steps 7 and 8 until the cluster assignments do not change (or the maximum number of iterations is reached).

Thus, a centroid for each cluster is assigned and the datapoints are assigned to each cluster based on the shortest distance between the cluster centroid and each datapoint. The entire procedure is carried out in MATLAB®, however, without the aid of the default k-means++ algorithm in the toolbox. A separate program with multiple call functions was written for the easy accessibility and modifiability based on the user requirements.

To select the optimum number of clusters, DBI index was used. The direct DBI clustering evaluation from the MATLAB® package was used to calculate the index for the clusters $k = 1$ to 6. The optimum cluster is the one with the lowest DBI value (Roundi et. al (16)). Based on the results, the optimum cluster was selected prior to executing k-means++ algorithm.

2.5. b-value characteristics for metal specimens

Recently, Botvina and Tyutin (2019) formulated a new acoustic parameter called acoustic gap to characterize the AE counts and energy recorded during cyclic load of metal specimens. They found the AE data from the metal specimens has the characteristics similar to the Gutenberg-Richter relation of the seismic events. They also have formulated the characteristics of the b-value under cyclic loading. However, the b-value of the AE data has a different characteristic under static loading conditions. The damage mode in the static tests vary significantly from the cyclic events and hence the b-value (b_{AE}) also varies. Based on this assumption, when formulated, there exists a linear relation between the natural logarithms of cumulative acoustic counts (N) and cumulative acoustic energy.

$$\ln \Sigma N = b_{AE} \ln \Sigma E \pm \text{int} \tag{2}$$

This relation exists not only in the AE data recorded in metal specimens but in almost all materials. The authors have observed this linear relation in different types of specimens. The slope b_{AE} value has been calculated and plotted over time. Based on the general damage progression in brittle materials, it is possible to relate the trend of the b_{AE} curve and the damage mode. The b_{AE} curve was plotted for all the specimens and the results were discussed in the subsequent sections.

2.6. Wavelet Transform of AE signal-based data

Although many researchers have used the AE parameter-based data such as AE counts and energy, the signal-based data has rarely been explored for metal specimens. The signal-based data has the inherent advantage over the parameter-based data on the basis that they filtered of any noises by passing them through a couple of band-pass filters. Moreover, these signals are not amplified and carries the close-to-true information of the AE waveform. Nonetheless, only a countable number of researchers have used the AE signal-based data in Continuous Wavelet Transform (CWT), Discrete Wavelet Transform (DWT) and Wavelet Packet Transform (WPT). All these research works were carried out on entirely different testing methods or applications. So far from the literature review made, this is the first time the wavelet transform has been used on static tests in metal specimens. The authors have used both the CWT and WPT using the Wavelet Toolbox in MATLAB® for this study. The time-frequency analysis was performed, and the different damage modes were related to the frequency content of the AE waves. For CWT, the analytical Morlet wavelet was used. The Morlet wavelet offers a better detection and localization of the AE events in the time-frequency domain compared to the conventionally used Morse of Bump wavelet (Mi et. al (2005)). Figure 1 shows the Morlet Wavelet.

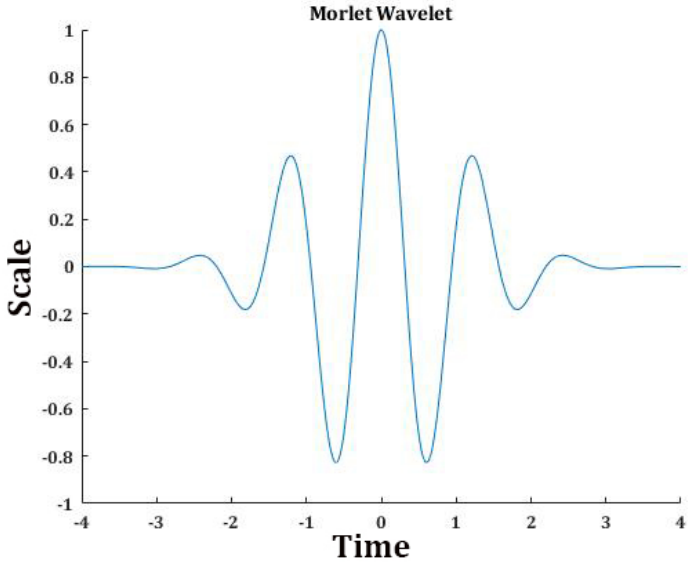

Fig 1. Morlet Wavelet.

This wavelet was shifted over the AE waves recorded during the testing and the CWT results are presented in the subsequent sections. The number of octaves during the shifting process was set as ‘2’ and number of voices per octaves was set as ‘32’. The number of octaves and voices per octaves are set based on the operating frequency of the AE sensor so that the entire frequency domain can be observed in the CWT results.

The WPT process decomposes the recorded wave into different frequency levels. This means that a recorded waveform is decomposed into low-frequency (approximation) and high-frequency (details) components. Then these

levels are further decomposed into their approximation and details. The process is continued for the predefined set of discrimination levels (l). The total number of components obtained from the WPT results is 2^l. In the present study, the decomposition level was set to 3, thereby obtaining 8 components.

3. Results

3.1. Tensile Test Results

Three specimens were tested for this study: T_X, T_Y, and T_{45}. The tensile test results, yield strength (σ_Y), ultimate tensile strength (σ_{UTS}), Young's modulus (E) and elongation at break (ε) are presented in Table 4. The σ_{UTS} corresponds to the peak load at the time of specimen failure.

Table 4. Tensile Test Results of all three Specimens

Specimen	**Yield Strength σ_Y**	**Ultimate Tensile Strength σ_{UTS}**	**Young's Modulus E**	**Elongation at Break ε**
Name	*MPa*	*MPa*	*GPa*	*%*
T_X	131.7	207.9	64.9	10.8
T_Y	136.9	214.5	65.8	12.6
T_{45}	124.5	214.2	63.5	10.7

3.2. Acoustic Emission Results

3.2.1. k-means++ clustered Results

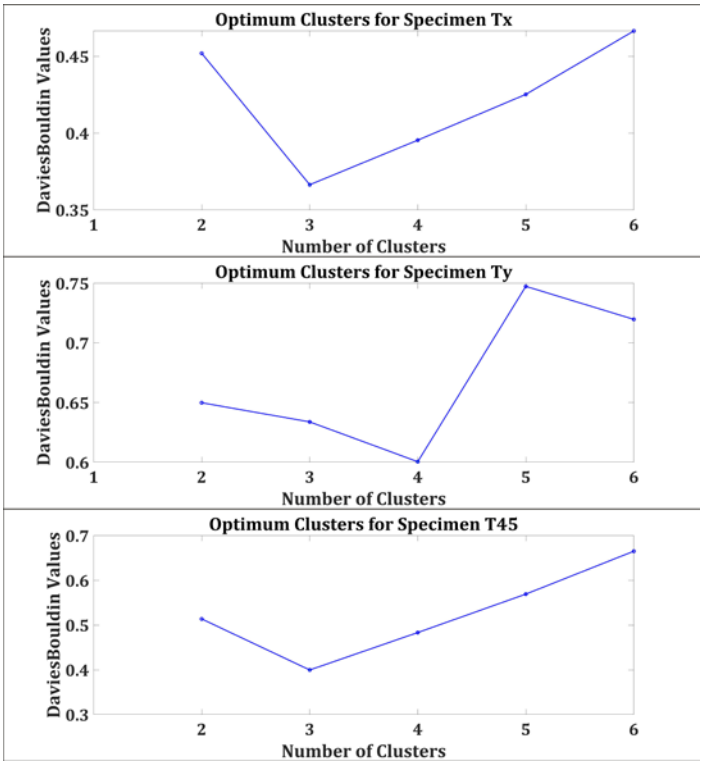

Fig 2. DBI Indices for Peak Amplitude data of all three Specimens

The peak amplitude, acoustic energy and counts were recorded for all three specimens. However, the peak amplitude was classified into different clusters. Before clustering using k-means++ algorithm, the DBI index was calculated to identify the optimum value of clusters into which the data can be classified. The DBI index for all the specimens is provided in Figure 2. The DBI indices are relative and it cannot be compared with different data sets. The minimum value of DBI index in each dataset with respect to the cluster (k) value must be considered as the optimum. The peak amplitude clustered using k-means++ algorithm for all three specimens are presented in Figure 3.

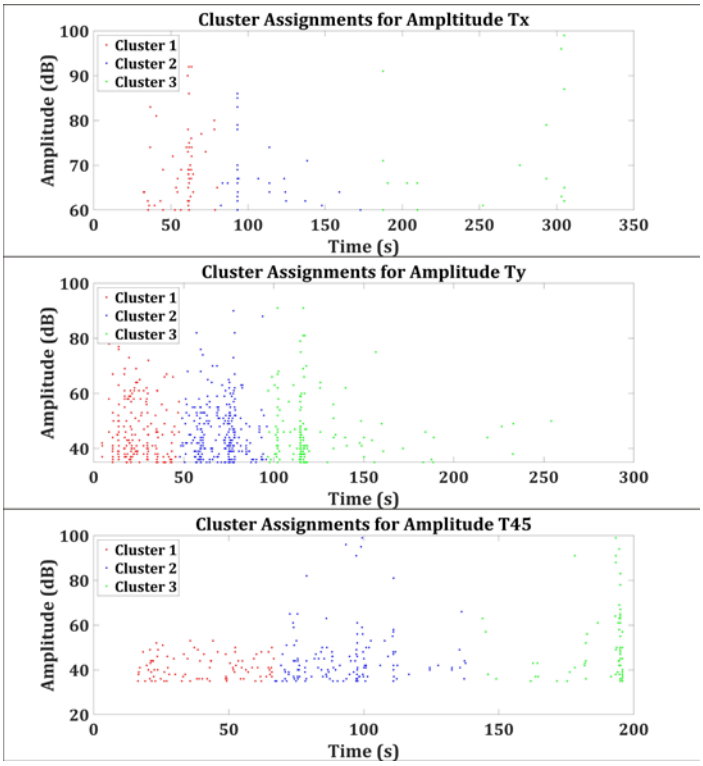

Fig 3. Amplitude data for all three Specimens classified using k-means++ algorithm.

3.2.2. b_{AE} Characterization Results

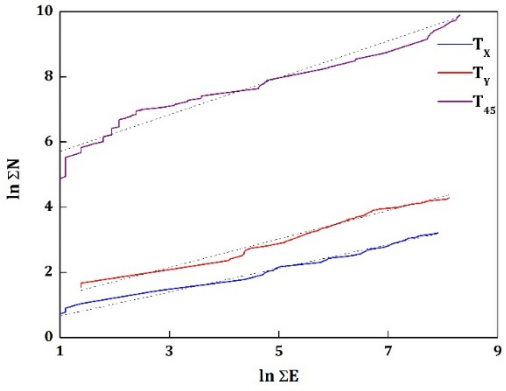

Fig 4. Linear relation between ln ΣN and ln ΣE

The linear relation between the natural logarithms of cumulative energy and the cumulative counts are presented in Figure 4. The b_{AE} value was calculated from this relation (Eqn. 2). Supposedly, the natural logarithms of counts and energy are in linear. Any discrepancies in the acoustic event generated under the loading conditions or different damage modes will affect this linearity. Thus, by estimating the value of the slope at all the points, these discrepancies can be identified. For successful assignment of the b_{AE} trend with the discrepancies, b_{AE} was plotted over time and presented in Figure 5.

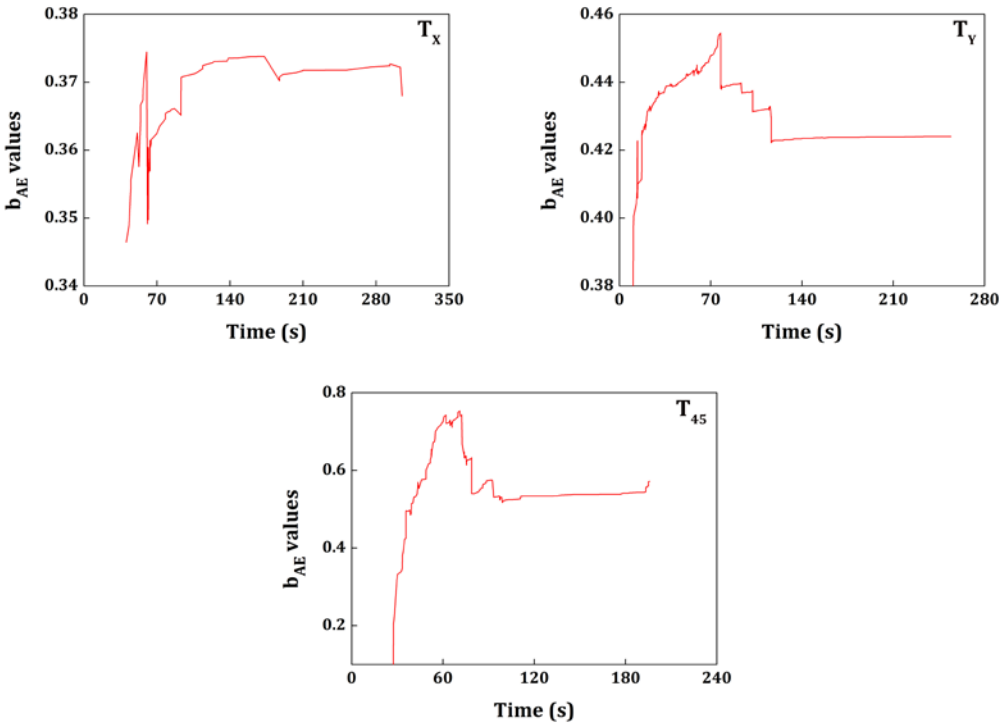

Fig 5. b_{AE} vs Time for all three Specimens

3.2.3. Wavelet Transform Results

Two AE signals from each cluster, one lower amplitude signal (<65 dB) and one higher amplitude signal (>65 dB) were taken for analysis. In specimen T_{45}, since there are no higher amplitude signals in cluster 1, the higher and lower amplitude signals are considered with respect to its limits. Thus, for each specimen, a total of 6 AE signals were analysed using both CWT and WPT waveform. The CWT results provides detailed information on the time-frequency domain, while the WPT results provide the energy content on different frequency levels. The CWT and WPT results of the waveforms recorded during the testing of T_X, are presented in Figure 6 and 7, respectively.

Both in the CWT and WPT results, the results in the first row of each figure represent the low amplitude signals and second row represents the higher amplitude signals. The first two columns from the left-hand side represent the cluster 1 and so on.

Similarly. the CWT and WPT results of the waveforms recorded during the testing of *Ty*, are presented in Figure 8 and 9, respectively. And the CWT and WPT results of the wavelets from specimens T_{45}, respectively, are presented in Figures 10, 11.

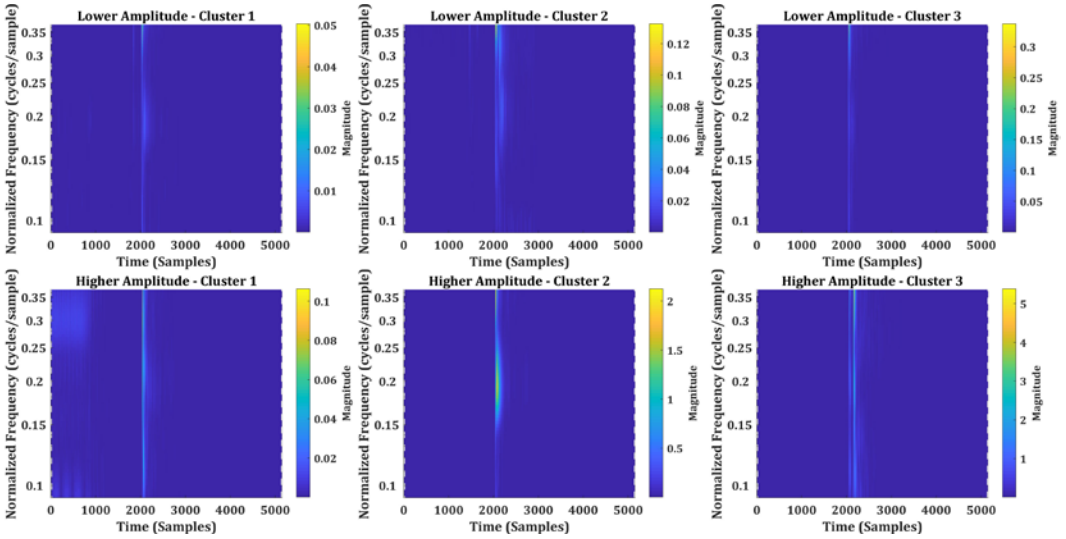

Fig 6. CWT results of the AE signals recorded in Specimen T_X

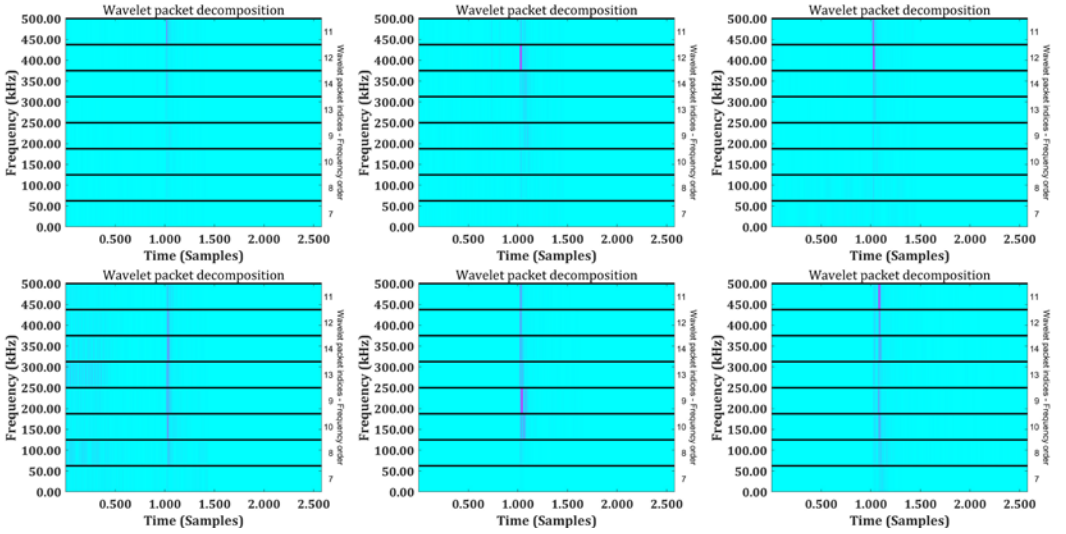

Fig 7. WPT results of the AE signals recorded in Specimen T_X

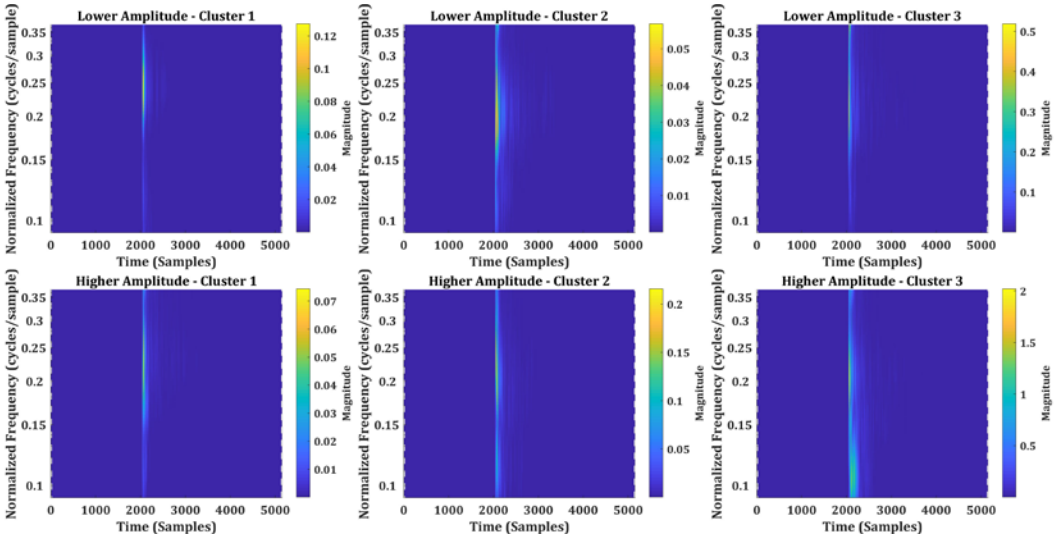

Fig 8. CWT results of the AE signals recorded in Specimen T_Y

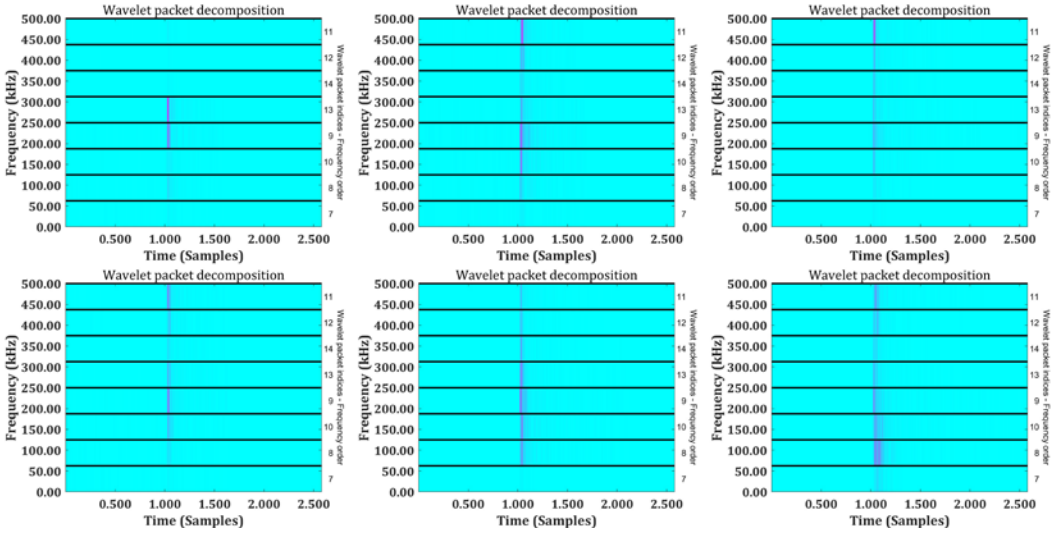

Fig 9. WPT results of the AE signals recorded in Specimen T_Y

To summarize the results section, the peak amplitude recorded during the acoustic events are used as the input data for k-means++ clustering. Whereas, the cumulative counts and cumulative energy are used to calculate the b_{AE} value. The signal-based data, the acoustic waveforms, are used for CWT and WPT analysis.

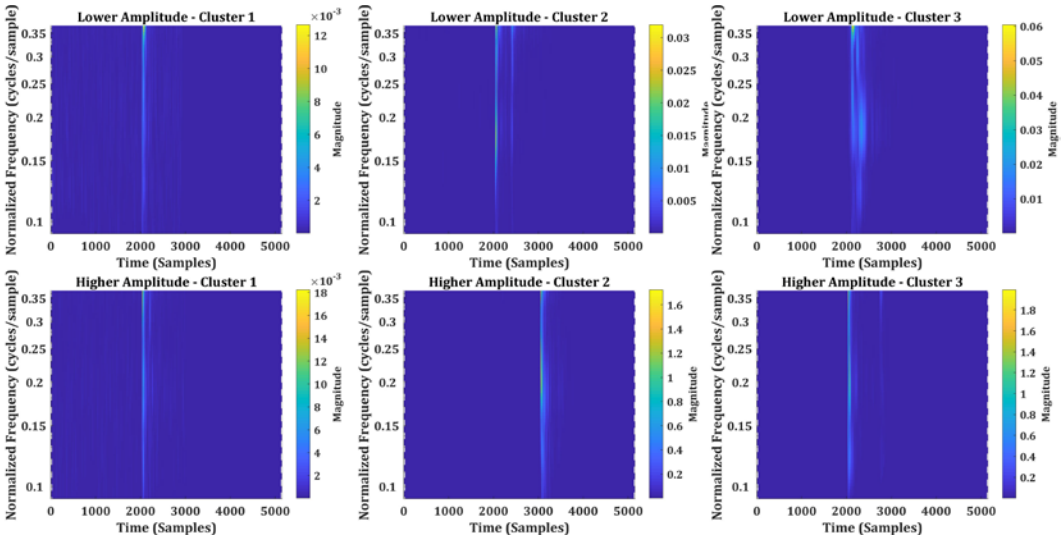

Fig 10. CWT results of the AE signals recorded in Specimen T_{45}

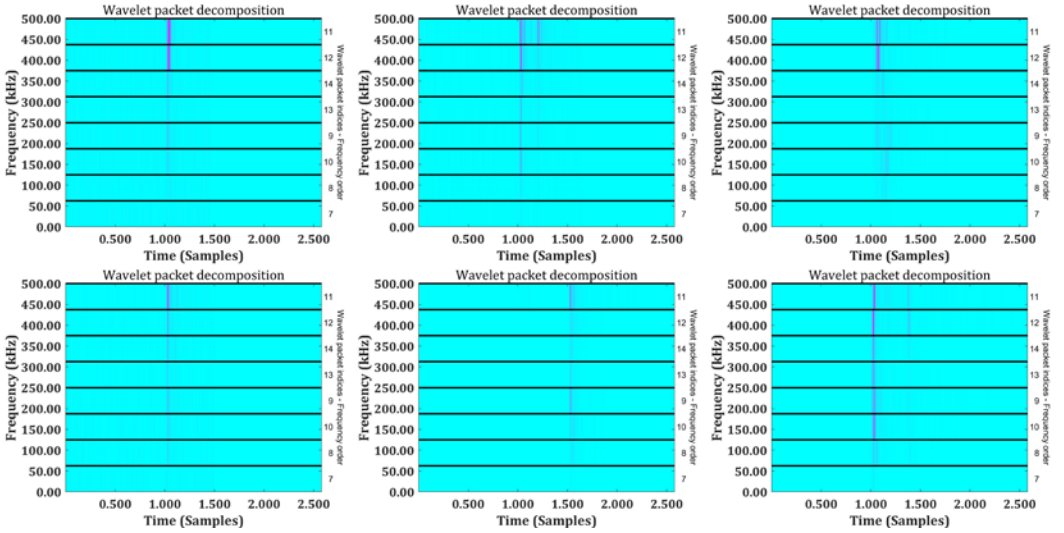

Fig 11. WPT results of the AE signals recorded in Specimen T_{45}

4. Discussions

The mechanical results for all the three specimens do not vary widely between each other, although T_Y specimen has a slightly lower peak load in comparison with the other specimens. The Young's modulus (E) and the yield strength (σ_Y) of the specimens built along X, Y and 45° orientation are comparable with the previous works done on the same material. The variation of the E and σ_Y of the three specimens is 1.16 GPa and 6.23 MPa, respectively. Moreover, the average values of E and σ_Y are also comparable with the previous literature works by Kempen et. al (2012) and Tradowsky et. al (2016). However, the elongation at break (ε) and ultimate tensile strength (σ_{UTS}) differ from the works by Kempen et. al (2012) and Tradowsky et. al (2016). The elongation at break from the previous literature works were reported to be between 3.5% to 5% Kempen et. al (2012) and Tradowsky et. al (2016), Wang et. al (2019) and Ch et. al. (2019), however, in our presented results it is between 10.7% to 12.6%. The post-processing of the SLM components such as hot isostatic compression or post heating treatment will reduce porosity of the final

component. This improves σ_{UTS} of the SLM component but at the same time reduces ε, since the material becomes slightly brittle after post-processing. In the present study, the SLM specimens are not post processed, thus having slightly lower σ_{UTS} and higher values of ε. The main objective of this study is to understand and relate the mechanical properties with different acoustic parameters, thus the post-processing was not considered. This leads to the presence of both surface and volumetric pores in the specimens. Moreover, the reduction in the scanning velocity near the border of the specimen creates more borderline porosity. These borderline porosities could possibly act as the crack initiator once the material reaches the yield point, leading to the early failure. The energy required for the failure of material beyond the crack initiation point is greatly reduced due to the brittle nature of the AlSi10Mg. This probably is the reason for the lower σ_{UTS} values of the AlSi10Mg specimens with respect to the previous literature works.

Beyond this point, there does not seem to be any major differences in the material properties or the damage modes while looking at the mechanical results. However, the change in orientation of the build direction can lead to variation in the material characteristics and their properties. Then concealed information are not apparent through the mechanical results. Thus, the aid of acoustic emission technique has been sought in this research work.

Initially, the DBI index was calculated for the cluster values of $k = 1 - 6$, for the peak amplitude values recorded during the testing of all three specimens. Figure 2 shows the DBI index of all three specimens. The lower the DBI index is the optimum number of clusters. While observing Figure 2, the DBI index of T_X and T_{45} have their minima at cluster 3, whereas T_Y has the minimum at cluster 4. Classifying the peak amplitude data on this basis will make it difficult for the comparison of all three specimens. The DBI index of specimen T_Y for the clusters 3 and 4 does not have a significant difference. Based on this factor the optimum cluster was taken as $k = 3$.

The peak amplitude data was classified into three clusters as per the DBI index, using k-means++ algorithm. The clustered results of all three specimens are provided in Figure 3. The classification clearly indicates that the damage propagation in all the three materials occurred in three different modes which are expressed in the clusters. Two particular information about the clustered results are intriguing. The first one is the duration of each clusters in different specimens and the second one is the distribution of peak amplitude in each cluster. In specimen T_X, the cluster one is between 0-80s duration whereas in T_Y it is only between 0-50s and in T_{45} it goes slightly beyond 65s. Similarly, the duration of second cluster/second damage region in specimen T_Y is narrow when compared to T_X and T_{45} results. Conversely, the third cluster/third damage region of T_{45} is narrow when compared to T_X and T_Y results. This shows that the duration of different damage modes is not similar in all the specimens.

The distribution of peak amplitude in each cluster is more intriguing. In cluster 1 of T_{45} specimen, no peak amplitudes above 55 dB can be observed, while T_X and T_Y have a significant amount of higher amplitude signals. However, number of higher amplitude signals can be observed in cluster 2 of specimen T_{45}, which are considerably larger in quantity than the cluster 2 of specimens T_X and T_Y. Cluster 3 of all three specimens are interesting in a way that there is a wider acoustic gap in specimen T_X at the beginning of cluster 3 and has signals of varying amplitude accumulated at the material failure zone. The similar observation can be observed in specimen T_{45} as well. However, in specimen T_Y, the signals are accumulated at the beginning of cluster 3, followed by a period of low acoustic activity. It is a well-known fact that different damage modes in a material can generate different amplitudes of acoustic signals. However, no literatures have been produced earlier to relate the amplitude or frequency of AE signals with the different damage modes in metals. Nonetheless, the results clearly indicated that all three materials took different damage paths before failure. In this research work, to relate these damage modes with the acoustic activities, the b_{AE} value and the signal-based (CWT and WPT) results are discussed.

Figure 8 shows the existing relation between the natural logarithms of cumulative counts and acoustic energy. This linear relationship can be observed not only in quasit-brittle materials such as concrete but also in metals and polymer composites. Based on this phenomenon, the b_{AE} relation has been created. Any anomalies in the acoustic events, leading to the huge energy bursts or lower acoustic activity could lead to the misalignment in this linearity. These anomalies can be identified by the slope (b_{AE}) at each point of the acoustic activity. Essentially, the b_{AE} can be directly related to the different damage modes.

In Figure 9, the plot between b_{AE} and the time for all three specimens are provided. The following hypotheses were made to characterize the damage modes in the metal specimens.

- When the b_{AE} value increases rapidly, large number of acoustic counts are recorded with lower energies. This represents the microcracking in the material.

- When the b_{AE} value increases gradually, the number of acoustic counts is larger, nonetheless, the energies of these events are also higher in comparison. This represents the yielding in the material, which generates more energy than the microcracking events.
- When the b_{AE} value decrease rapidly, fewer acoustic counts are recorded with higher energies. This represents the crack opening and crack propagation, which generally produces acoustic events with higher energies. In the meantime, this could also represent crack path propagating through the volumetric or surface pores/defects.
- When the b_{AE} value remains constant, then the material has lost its load carrying capability and progressing towards failure.

Now comparing these hypotheses created with the Figure 9, the different damage modes can be identified.

In specimen T_X, the microcracking has occurred in a very short period of time, but at the same time, a sudden drop in b_{AE} value can be seen between the two consecutive rapid increase. This is followed by a sudden drop in the b_{AE} value exemplifying the crack opening. However, this possibly could represent the relaxation of the volumetric or surface pores which resulted in sudden energy bursts but without deteriorating the material property. This is followed by a gradual increase until 90s duration, followed by a small drop in b_{AE} value. Following another sudden increase in b_{AE} value, the yielding occurs until 200s duration (approximately). A drop at this point signifies the major damage in the material and beyond this point, the b_{AE} value remains constant until the material failure.

In specimen T_Y, the b_{AE} increases gradually before it reaches 70s duration and a quick exponential growth can be seen at this point, followed by multiple sudden drops in the b_{AE} value. The duration between each of these drops are very narrow indicating that this probably could be the crack growth and each time the crack propagates through a surface or volumetric pore, there is a sudden drop in b_{AE}. The b_{AE} value remains constant beyond the final drop indicating that the final major drop is the point where the material started losing its load bearing capability. It also could be noted that the gradual increase in the b_{AE} value from 10s to 70s duration indicates the yielding of the material. The yielding trend of b_{AE} is wider in T_Y than in any other specimens. Coincidentally, the elongation at break of T_Y is slightly larger than the other specimens, supporting the hypotheses created.

In the specimen T_{45}, the crack path propagates through less pores than in specimen T_Y. This indicates that, although the tensile results showed that the materials do not have any significant difference between each other, the b_{AE} curve proved to be different. The different damage modes can be viewed through the b_{AE} curve.

Each wavelet is recorded for every acoustic event recorded. It is, however, impossible to analyse few hundreds of wavelets using CWT or WPT. For this purpose, a total of 6 wavelets, two wavelets (one lower amplitude and one higher amplitude) from each cluster was taken for this study. Figure 6 shows the CWT results of specimen T_X. All the wavelets recorded are very transient and has a very low duration. Unlike the acoustic signals of polymer composites or concrete structures, the metal specimens generate very narrow signals. Observing the Figure 6, the noise signals of longer duration can be seen in the lower amplitude cluster 2 results. If the peak amplitude is considered for analysis, it normally can capture the noise signal which is why the histogram of the wavelets must be analysed. The maximum magnitude of the lower amplitude signals is in the range of 0.05, 0.1 and 0.12 in cluster 1, 2 and 3, respectively. At the same time, the maximum magnitude of higher amplitude signals is 2, 0.3 and 5, respectively for cluster 1, 2 and 3. The higher amplitude in cluster 2 is really insignificant because it has lower magnitude when compared to the other two clusters and it is barely visible in the time frequency domain. It could have been considered significant if the magnitude is higher. For instance, the magnitude of higher amplitude signal in cluster 3 is 5, even though it is associated with some noise signals. The higher amplitude signal in cluster 1 could possibly represent the energy burst responsible for sudden drop in b_{AE} value at the early stage.

Now by observing Figure 7, the WPT of T_X, the frequency of the signal responsible for the drop in b_{AE} value can be observed. It is centred around 195-245 kHz. The frequency of the higher amplitude signals in cluster 2 and 3 are in 390-440 kHz and 440-488 kHz domain. This clearly indicates that despite the sudden energy burst, the responsible damage mode is different in each mode.

In Figure 8, the CWT results of T_Y specimen are presented. It was observed in Figure 7 that a number of higher amplitude signals are distributed throughout cluster 1 and 3 in specimen T_Y. However, there are a few higher amplitude signals in cluster 2 as well. Looking at the CWT results, it shows that the maximum magnitudes of these signals are much lower when compared to the CWT results of T_X. In cluster 3, however, the signal is saturated over a longer duration with respect to the time. The signals are not of shorter duration as their counterparts. This possibly could indicate that the location of the acoustic events in cluster 3 are not closer to the other acoustic events. This is the reason

behind the longer duration signals. It was also observed in Figure 9 that the b_{AE} value had several drops (representing crack propagation path through pores). This indicates that the crack path was different in specimen T_Y than in specimen T_X.

The WPT results in Figure 9 shows that there are two significant frequency bands in lower amplitude cluster 1 signal. Three significant frequency bands can be seen in lower amplitude cluster 3 signals.

The CWT results of specimen T_{45} in Figure 10 shows that the magnitude of the signals is very low. This is also due to the fact that no signals above 65 dB is recorded in cluster 1 of T_{45}. The signals in cluster 3 of lower amplitude seems to be saturated to a longer duration, however, comparing it with Figure 11 clearly indicates that the significant signals are centred around 390-440 kHz and 440-488 kHz frequency bands. The remaining are probably noise signals. The frequency bands are much similar to the bands observed in T_X CWT and WPT results. This is also another reason why the higher amplitude in cluster 3 were similarly distributed in specimens T_X and T_{45} (Figure 3).

These results are significant enough to prove the hypotheses provided, nonetheless, the future scope for this area is vast. If the material characteristics is recorded under multiple evaluation sources such as drop voltage or in-situ microscopic analysis, the damage modes and the frequency bands associated with each damage mode can directly be related with the acoustic emission results. Acoustic emission can be implemented successfully in analysing the integrity of large structures.

5. Conclusions

Three SLM specimens were prepared in different orientations of the building platform. The mechanical results show that the properties of the materials built in different platforms do not vary from each other. However, the acoustic emission results proved otherwise. The peak amplitude of the acoustic signals was clustered using k-means++ algorithm to identify the different damage regions. The cumulative energy and cumulative counts of the acoustic events were successfully used to evaluate the b_{AE} parameter. A set of hypotheses was created to relate the damage mechanisms with the b_{AE} trends over time. Finally, the different damage was characterized in time-frequency domain using WPT and CWT analysis. The results showed that the acoustic emission is a powerful tool in characterizing damage progression. This novel approach has a wider scope for expansion in the very near future.

References

ASTM E8 / E8M-13, Standard Test Methods for Tension Testing of Metallic Materials, ASTM International, West Conshohocken, PA, 2013, www.astm.org

Barile, C., Casavola, C., Pappalettera, G., Pappalettere, C., 2014. Hybrid thermography and acoustic emission testing of fatigue crack propagation in Aluminum Samples. In: Conference Proceedings of the Society for Experimental Mechanics Series, 247–252.

Barile, C., Casavola, C., Pappalettera, G., Pappalettere, C., 2015. Fatigue Damage Monitoring by Means of Acoustic Emission and Thermography in Ti Grade 5 Specimens. Procedia Engineering, 114, 487–492.

Bi, H., Li, Z., Hu, D., Toku-Gyamerah, I., Cheng, Y., 2015. Cluster analysis of acoustic emission signals in pitting corrosion of low carbon steel. Materialwissenschaft Und Werkstofftechnik, 46(7), 736–746.

Botvina, L.R., Tyutin, M.R., 2019. New acoustic parameter characterizing loading history effects. Engineering Fracture Mechanics 210, 358-366.

Carpinteri, A., Lacidogna, G., 2007. Damage evaluation of three masonry towers by acoustic emission. Engineering Structures 29(7), 1569–1579.

Ch, R.R., Raja, A., Nadig, P., Jayaganthan, R., Vasa, N.J., 2019. Influence of working environment and built orientation on the tensile properties of selective laser melted AlSi10Mg alloy. Material Science and Engineering A – Structural Materials: Properties, Microstructure and Processing 750, 141-151.

Chai, M., Zhang, J., Zhang, Z., Duan, Q., Cheng, G., 2017. Acoustic emission studies for characterization of fatigue crack growth in 316LN stainless steel and welds. Applied Acoustics, 126, 101–113.

Everson, C.E., Cheraghi, H.S., 1999. The application of acoustic emission for precision drilling process monitoring. International Journal of Machine Tools and Manufacture 39(3), 371–387.

Finkel, P., Mitchell, J.R., Carlos, M.F., 2000. Experimental study of 'Auto Sensor Test-Self Test Mode' for acoustic emission system performance verification. AIP Conference Proceedings 509, 1995–2002.

Grosse, C., 2008. Introduction. In: Acoustic Emission Technique, Grosse, C, Ohtsu, M. Springer, Berlin, Heidelberg.

Kempen, K, Thijs, L, Van Humbeeck, J, Kruth, J.P., 2012. Mechanical properties of AlSi10Mg produced by Selective Laser Melting. Physics Procedia 39, 439 – 446.

Mi, X., Ren, H., Ouyang, Z., Wei, W., Ma, K., 2005. The use of the Mexican Hat and the Morlet wavelets for detection of ecological patterns. Plant Ecology 179(1), 1–19.

Minak G., Zucchelli A., 2008. Damage evaluation and residual strength prediction of CFRP laminates by means of acoustic emission techniques. In: Composite Materials Research Progress, Lucas P. Durand, Nova Publishers, 165-207.

Pascoe, J.A., Zarouchas, D.S., Alderliesten, R.C., Benedictus, R., 2018. Using acoustic emission to understand fatigue crack growth within a single load cycle. Engineering Fracture Mechanics 194, 281–300.

Roundi, W, Mahi, A.E., Gharad A.E., Rubiere, J., 2018. Acoustic emission monitoring of damage progression in Glass/Epoxy composites during static and fatigue tensile tests. Applied Acoustics 132, 124-134.

Tradowsky, U., White, J., Ward, R.W., Read, N, Reimers, W., Attallah, M.M., 2016. Selective laser melting of AlSi10Mg: Influence of post-processing on the microstructural and tensile properties development. Materials & Design 105, 212-222.

Vshivkov, A.N., Iziumova, A.Y., Panteleev, I.A., Ilinykh, A.V., Wildemann, V.E., Plekhov, O.A., 2019. The study of a fatigue crack propagation in titanium Grade 2 using analysis of energy dissipation and acoustic emission data. Engineering Fracture Mechanics 210, 312-319.

Wang, P., Lei, H., Zhu, X., Chen, H., Fang, D., 2019 Influence of manufacturing geometric defects on the mechanical properties of AlSi10Mg alloy fabricated by selective laser melting. Journal of Alloys and Compounds 789, 852-859.